Results in Engineering 26 (2025) 105286

Contents lists available at ScienceDirect

Results in Engineering

journal homepage: www.sciencedirect.com/journal/results-in-engineering

Developing a novel non-destructive method to monitor relative humidity at the steel-concrete interface using RFID-MEMS sensors

Jia-Xiang Liew [a,b,*], Hong Wong [a,*]

[a] Centre for Infrastructure Materials, Department of Civil and Environmental Engineering, Imperial College London, United Kingdom
[b] Department of Civil and Environmental Engineering, The Hong Kong Polytechnic University, Kowloon, Hong Kong, China

ARTICLE INFO

Keywords:
Steel-concrete interface
Relative humidity
RFID
MEMS sensor
Reinforcement spacer

ABSTRACT

Moisture at the steel-concrete interface (SCI) can influence the durability of reinforced concrete but a fundamental understanding of its effects on corrosion initiation and propagation remains inconclusive. This is partly due to a lack of reliable, non-destructive monitoring techniques. This study introduces a novel approach leveraging 3D-printed reinforcement spacers with embedded RFID-MEMS sensors to enable in situ, real-time relative humidity monitoring at the SCI. Concrete specimens with different water-to-cement ratios (0.40, 0.55) and curing ages (3, 14 days) were exposed to 50 °C and 65 % RH, 21 °C to produce varying degrees of porosity and moisture content. The results show that precise measurements with a maximum difference of ± 2 % can be obtained for exposure humidity up to 90 % RH. However, a reduction in precision occurred above 93 % RH due to condensation effects. Crucially, this work demonstrates the first successful integration of RFID-MEMS sensors in 3D-printed spacers to quantify SCI moisture states non-destructively, providing actionable insights for corrosion risk assessment tailored to concrete composition and environmental exposure.

1. Introduction

Moisture in concrete, and particularly at the steel-concrete interface plays a critical role in the durability and service life of reinforced concrete structures. For example, carbonation reaches a maximum rate when the relative humidity of the exposure environment is between 50 and 70 % [1–4]. At lower relative humidity, chemical reactions between calcium-bearing constituents and gaseous CO_2 are limited by moisture deficiency [5]. Moisture containing chlorides increases the risk of corrosion and buffers the pH during early pitting corrosion. Partially saturated conditions have a higher oxygen supply and accelerate rate of corrosion [6–10]. Despite the critical dependence on moisture, current understanding of SCI moisture dynamics remains incomplete, primarily due to the lack of reliable in situ monitoring techniques capable of providing accurate, real-time measurements without compromising structural integrity.

Existing approaches for moisture monitoring face significant limitations. While non-destructive techniques such as microwave impulse devices [11], ground-penetrating radar [12] and nuclear magnetic resonance sensors [13] offer valuable insights, they are typically limited to control laboratory conditions. Embedded sensors, including four-point probe [14]' low calcium fly ash geopolymer sensor [15], and MEMS devices [16] can provide direct measurements but could disrupt the surrounding microstructure of concrete, potentially compromising data reliability. For example, these techniques can induce additional voids in the cementitious matrix, altering the chloride threshold limit [17]. Furthermore, conventional sensors frequently suffer from measurement drift due to material hysteresis [18]' temperature sensitivity [19–21]' and limited resolution in cementitious environments [22,23]. These constraints highlight a critical technological gap with the need for a minimal invasive monitoring system that can provide reliable moisture measurements at the SCI without disrupting the local microstructure or requiring destructive sampling.

Radio-Frequency Identification (RFID) is a wireless technology that uses electromagnetic fields to automatically identify, and track tags attached to objects. Unlike traditional methods, RFID does not require line-of-sight scanning, enabling faster, more efficient data collection. RFID systems consist of a reader (transceiver), an antenna, and a tag (transponder), which can be passive (powered by the reader's signal) or active (battery-operated). This technology is widely adopted in supply chain management, access control, and retail inventory systems due to its ability to handle large-scale, automated tracking. Recent

* Corresponding authors.
E-mail addresses: jxliew@polyu.edu.hk (J.-X. Liew), hong.wong@imperial.ac.uk (H. Wong).

https://doi.org/10.1016/j.rineng.2025.105286
Received 22 April 2025; Received in revised form 8 May 2025; Accepted 10 May 2025
Available online 11 May 2025

advancements in RFID, particularly when integrated with Micro-Electro-Mechanical Systems (MEMS), have expanded its applications into structural health monitoring and environmental sensing [24–28]. High-frequency (13.56 MHz) RFID-MEMS systems, for instance, demonstrate significantly greater longevity than ultra-high-frequency (UHF) alternatives, maintaining functionality for over 1000 days in harsh cementitious environments [29,30]. Their durability makes them ideal for long-term embedded sensing in infrastructure, such as bridges and buildings, where maintenance access is limited. A key innovation is the integration of these sensors with 3D-printed enclosures, allowing them to function both as reinforcement spacers in concrete and as real-time monitoring devices. This minimizes disruption to the surrounding microstructure while providing critical data on saturated and partially saturated states, while the on-chip temperature compensation algorithms can effectively decouple thermal effects from moisture measurements, enhancing reliability under varying environmental conditions.

By addressing the key limitations of existing methods including microstructural disruption, measurement drift and temperature sensitivity this study advances the fundamental understanding of moisture dependent mechanisms while providing a practical tool for structural health monitoring. The proposed method, which function both as a structural component and a sensing platform, represents a significant advancement toward intelligent infrastructure capable of autonomous durability assessment.

This study introduces a novel SCI monitoring method through the development of:

a) 3D-printed reinforcement spacers with embedded 13.56 MHz RFID-MEMS sensors designed to comply with BS 7973–1 standards [31] for mechanical performance.
b) A wireless monitoring system capable of tracking RH variations at the SCI with ± 2 % precision up to 90 % RH.
c) Comprehensive validation across concrete mixture ($w/c = 0.4$, 0.55) and curing ages (3, 14 days) to establish sensor performance under controlled environmental exposures.

2. Methods

2.1. Materials and mix proportions

Concrete and mortar samples were prepared by using ordinary Portland cement (CEM I, 52.5R) as the primary binder, combined with locally sourced sand, graded gravel aggregates, and water. The mix proportions followed the predefined mixture design outline in Table 1, ensuring consistent water-to-cement (w/c) ratios. The key physical properties (including fineness, specific gravity and density) and detailed chemical composition (major oxides CaO, SiO_2, Al_2O_3 and Fe_2O_3) of the Portland cement are given in Table 2. Two water-to-cement (w/c) ratios of 0.4 and 0.55 were selected to produce concretes with different pore structures and strengths with at least two replicates for each sample. The total aggregate volume fraction was fixed at 50 % for the mortar and 70 % for concrete. Specific gravity, percentage of moisture absorption to saturated surface dry condition (SSD) and total evaporable moisture content of aggregates were measured with procedures provided by ASTM C566 and C128 [32,33] presented in Table 3.

2.2. Sensor selection and enclosure design

Various design and sensing requirements were considered prior to selecting an optimal relative humidity sensor for this study. Dimensions of electronic circuit boards should preferably be smaller than 50 × 50 × 50 mm to enable the sensors to be embedded in 3D-printed enclosures and achieve a range of practical cover depths [34]. The electrically erasable programmable read-only memory (EEPROM) will require a minimum of 1 Kbyte of data to allow users to monitor measurements on a regular basis. This is based on the expectation that relative humidity and moisture content fluctuate at a much slower rate in real structures (compared to the external environment) and therefore can be monitored at hourly intervals for at least 5 years until structural maintenance checks are required.[16,17] Additionally, measurements must be transmitted by wireless communication to avoid the need for physical (wired) connections that could affect the integrity of the concrete cover.

With the aforementioned requirements, it is also critical to consider the design and sensing specifications of the relative humidity sensors. This plays a crucial role in determining the feasibility of monitoring relative humidity at the steel-concrete interface. Dimensions of relative humidity sensors should preferably be smaller than 5 × 5 × 5 mm to accommodate a wide range of steel reinforcement including bars with a minimum diameter of 8 mm. Particularly, quantification within the millimetre range is required to characterize moisture content in macroscopic interfacial voids. Furthermore, for laboratory-based research, a response time of <60 s will be desirable to detect instantaneous changes in relative humidity. A sensing range between 10 and 90 % humidity is required to monitor the depassivation of steel during carbonation-induced and chloride-induced corrosion. By controlling the relative humidity of the exposure environment between 50 and 70 %, carbonation was found to reach a maximum rate [1]. At lower relative humidity, chemical reactions between calcium-bearing constituents and gaseous CO_2 are limited by a deficiency of moisture [5]. Furthermore, it was hypothesized that moisture conditions of interfacial voids will probably influence chloride-induced corrosion at the steel-concrete interface [35]. Completely saturated interfacial voids containing chlorides may potentially increase the risk of corrosion and buffer the pH during early pitting corrosion. Partially saturated interfacial voids will have a higher abundance of oxygen supply and accelerate the rate of corrosion. Lastly, the internal temperature of reinforced concrete structures can range between −5 to 40 °C during the summer and winter seasons [36,37]. Hence, sensors must be able to operate at a temperature range that exceeds this.

After a comprehensive search of available sensor technologies, STEVAL- SMARTTAG1 manufactured by ST Microelectronics was chosen for this study. It utilizes NFC (near field communication) Forum type V based on RFID technology and transmits/receives information over the 13.56 MHz wireless frequency range. Furthermore, the sensing element consists of a polymer dielectric planar capacitor structure with dielectric materials surrounded by a medium of low refractive indexes. The sensor is factory calibrated to have an accuracy of ± 3.5 % RH, deviation of ± 0.5 % RH per year, humidity hysteresis ± 1 % RH and sensitivity of 0.004 % RH/LSB (least significant bit) specified by the manufacturer. The overall dimensions consist of a 43 × 43 × 30 mm encasing and operates at a temperature range of −40 to 120 °C.

Subsequently, the 3D-printed enclosure was designed using SolidWorks with a groove of 9.5 mm in diameter (to hold the reinforcing steel bar). The CAD model was then exported in STL file format and imported

Table 1
Mix proportions.

Mix design	w/c ratio	Water (kg/m^3)	Sand (kg/m^3) <5mm	Coarse aggregate (kg/m^3) <10mm	Cement (kg/m^3)	Aggregate vol fraction: %
C-0.55-PC-70	0.55	189.1	719.4	1079.1	343.8	70
C-0.4-PC-70	0.40	166.1	719.4	1079.1	415.2	70
M-0.4-PC-50	0.40	280.6	1331.8	–	691.9	50

Table 2
Physical properties and chemical characteristics of the cement used.

Density (kg/m^3)	Fineness (kg/m^3)	Loss-on-ignation (%)	CaO (%)	SiO_2 (%)	Al_2O_3 (%)	Fe_2O_3 (%)	MgO (%)	K_2O (%)	Na_2O (%)	SO_3 (%)
3100	2910	2.1	63.43	20.80	5.43	2.40	1.51	0.70	0.30	2.9

Table 3
Aggregate properties.

Aggregate type	Maximum partice size: mm	Density (kg/m^3)	Moisture absorption: %	Moisture content: %
Fine	5	2664	1.05	0.24
Coarse	10	2510	2.0	0.37

to Ultimaker S5 Pro for printing, as illustrated in the schematic diagram of Fig. 1**(a)**. To prevent particulate contamination and provide a direct moisture measurement at steel surface without compromising sensor performance or structural integrity a 2 mm diameter hole was incorporated as shown in Fig. 1**(b)**. The bottom enclosure was embedded in a silicone mould to enable sensor retrieval without damaging the specimens with destructive methods. To test the design, concrete specimens of 100 mm diameter and thickness of 45 mm were cast in plastic moulds and compacted on a vibrating table until no significant release of air bubbles was observed. After compaction, specimens were covered with wet hessian fabric at room temperature for 24 hours to prevent drying. Upon retrieving the sensor, it was observed that no water or solid particulates had penetrated the enclosures. This shows that the enclosure was able to protect the sensors during concrete casting. Fig. 2 shows that the 3D-printed enclosure with the embedded sensor can be adopted for the specific purpose of monitoring relative humidity at the steel-concrete interface. The printed enclosure can be customized to produce spacers for different rebar sizes and cover depths.

2.3. Precision of MEMS sensors

The relative humidity measurement from each sensor was monitored

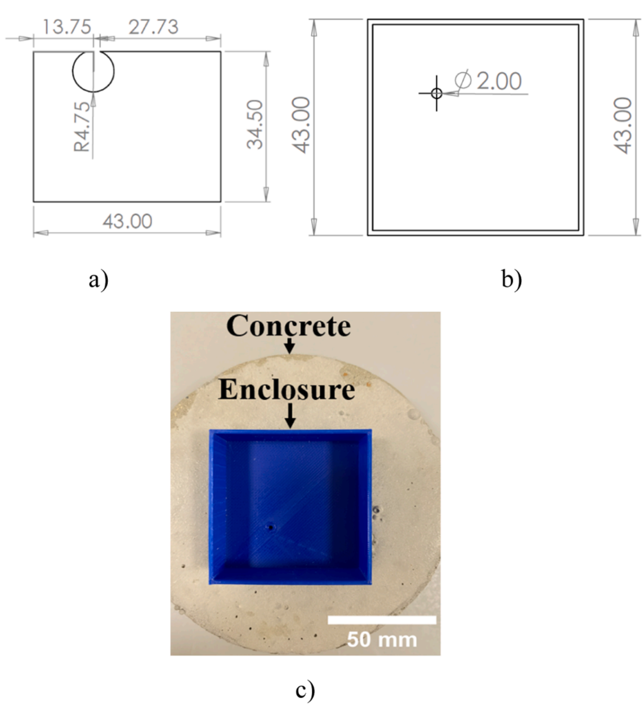

Fig. 1. a, b) Schematics showing the side (a) and bottom (b) view of the enclosure design with units in mm. c) Photograph showing the bottom view of the concrete sample with embedded sensor enclosure after 24 hours of curing.

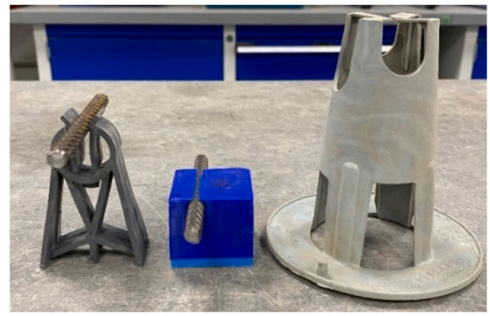

Fig. 2. Comparing the developed sensor enclosure for monitoring steel-concrete interface (centre) with commercially available reinforcement spacers: 50 mm plastic A-shaped spacer (left) and 100 mm plastic tower spacer (right).

in a temperature-controlled laboratory at 21± 2°*C* and 55± 5 % RH. In total, 30 individual sensors were tested and the maximum deviation was observed to be ± 1 % RH. Subsequently, the precision of MEMS sensors was tested with incubators at constant humidity of 75 % RH, 86 % RH, 93 % RH and 100 % RH. The constant humidity was achieved by using saturated sodium chloride (75 % RH), potassium hydrogen sulphate (86 % RH), potassium nitrate (93 % RH) salt solutions and moisture (100 % RH). Each incubator was conditioned with fresh salts for a week in a temperature-controlled laboratory at 21± 2 °C and relative humidity was monitored with a Fisherbrand Traceable thermometer and humidity sensor. The effect of moisture on the rate of response was examined by placing the RFID MEMS sensors in enclosures at increasing relative humidity, from 75 % RH to 86 % RH, 93 % RH and 100 % RH, for 15 min each and with measurements obtained every 5 s. In another set of experiments, RFID MEMS sensors were placed in incubators at decreasing relative humidity, from 100 % RH to 93 % RH, 86 % RH and 75 % RH, for 15 min with measurements obtained every 5 s to study the influence of condensation and stiction.

2.4. Wireless communication range

To examine the influence of concrete cover and moisture state on communication range, specimens with dimensions of 100 × 100 × 100 mm and 100 × 100 × 50 mm were prepared. Concrete (C-0.4-PC-70) and mortar (M-0.4-PC-50) were dry mixed in a pan mixer for 30 s and wet mixed for 3 min after the addition of water. Specimens were cast in plastic moulds and compacted on a vibrating table until no significant release of air bubbles was observed. Compacted specimens were covered with wet hessian fabric at room temperature for 24 hours to prevent drying, then demoulded and placed in a curing room at a temperature of 20 ± 2°*C* and relative humidity of 95 ± 5 % for 2 days.

Communication distance was determined by placing an RIFD MEMS sensor in a polyethylene terephthalate enclosure with the sensor and antenna surface in direct contact with the specimen shown in Fig. 3a. Note that the surface area of each specimen (100 × 100 mm) was greater than the sensor (43 × 43 mm) to minimize the effects of side leakage. Subsequently, electromagnetic waves were continuously emitted from the ST25R3911B-DISCO RFID reader with the continuous scan mode allocated on the ST25PC—NFC software. The reader was shifted at 5 mm increments until the RFID MEMS sensor was undetectable and the maximum communication distance was measured with a vernier calliper. In addition, specimens were submerged in tap water to a total

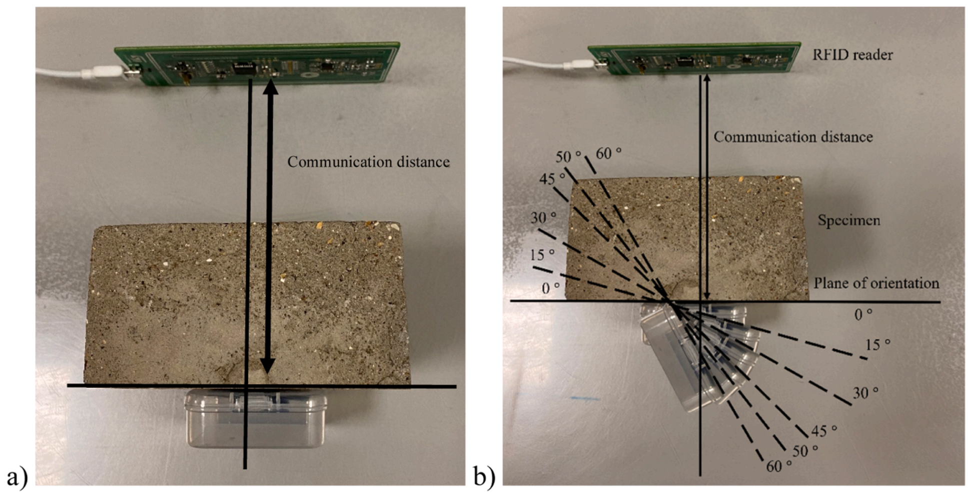

Fig. 3. Test method to determine the maximum communication distance by placing RFID MEMS sensor at different distances (a) and orientations (b) away from concrete and mortar specimens.

depth of 60 mm and 110 mm for 5, 15, 30 and 60 min to study the impact of moisture on wireless communication range. Further tests included placing the RFID MEMS sensor at 15°, 30°, 45°, 50° and 60° away from the plane parallel to the RFID reader to investigate the effect of directional placement on the communication range shown in Fig. 3b

2.5. Monitoring relative humidity

Fourteen cylindrical concrete specimens of 100 mm diameter and nominal cover depth of 25 mm were prepared. The concrete mixes (C-0.4-PC-70 and C-0.55-PC-70) were mixed, cast and compacted as described in the previous section. Before casting, the 3D-printed enclosures with attached 8 mm diameter steel bars were placed in the moulds and then filled with fresh concrete. Specimens were compacted on a vibrating table, covered with wet hessian at room temperature, demoulded after 24 hours, and cured at 20 ± 2 °C and 95 ± 5 % RH for 3 and 14 days. Subsequently, the sides of specimens were coated with epoxy and sealed with adhesive tape to ensure one-sided absorption and desorption shown in Fig. 4. Following this changes in relative humidity at the steel-concrete interface caused by drying and rewetting were monitored, the cured specimens were first dried in 50 °C oven for four weeks. Subsequently, they were placed in incubators containing saturated ammonium nitrate (65 % RH; 21 $^\circ C\pm$ 2 °C) until a mass change smaller than 0.01 % was obtained. This relative humidity was chosen to ensure that sensors could detect changes in moisture that are critical for carbonation.

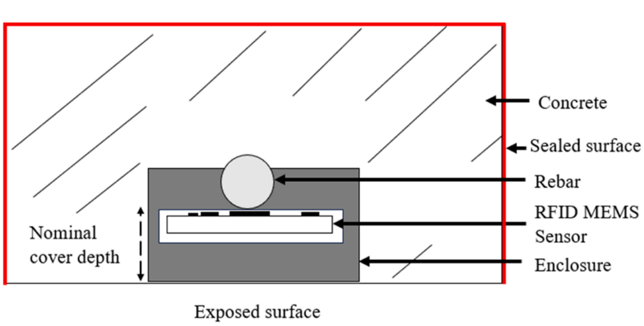

Fig. 4. Schematic diagram showing the reinforced concrete specimen with embedded RFID MEMS sensor in a 3D printed enclosure for monitoring steel-concrete interface.

2.6. Finite element modelling

Finite element modelling (FEM) was employed to simulate the drying process of the specimen, utilizing the geometric configuration and procedures detailed in Section 2.5. The FEM simulation was conducted using COMSOL Multiphysics, implementing a moisture transport model proposed by Sun et al. [38].. In this model, the primary variable is the saturation degree θ, governed by the equation

$$\frac{\partial\theta}{\partial t} = \nabla\cdot[D(\theta)\cdot\nabla\theta] \tag{1}$$

where $D(\theta)$ is the effective moisture transport coefficient, which can be determined through the capillary pressure p_c and vapour density ρ_v by

$$D(\theta) = -\frac{1}{\rho_l\phi}\left(D_v\frac{M_w\rho_v}{\rho_l RT} + K_l\right)\frac{\partial p_c}{\partial\theta} \tag{2}$$

In this equation, ρ_l is the density of liquid water; D_v and K_l are the diffusion coefficient of vapour and the permeability coefficient of liquid water in concrete, respectively; M_w is the molar mass of water molecules; R is the gas constant; and T is the temperature. The relationship between capillary pressure p_c and the saturation degree θ is defined by the water-vapour sorption isotherm (WVSI). In this study, the WVSI as suggested by Sun et al.[19] is adopted:

$$\begin{cases} \theta_w = 1 - \exp\left(\frac{2B\gamma\cos\alpha}{p_c}\right) \\ \theta_d = \left[1 - \exp\left(\frac{2B\gamma\cos\alpha}{p_c}\right)\right]\left\{1 - \ln\left[1 - \exp\left(\frac{2B\gamma\cos\alpha}{p_c}\right)\right]\right\} \end{cases} \tag{3}$$

where θ_w and θ_d are the saturation degrees during the drying and wetting processes, respectively; B is the pore size distribution-related parameter; γ is the surface tension of liquid water; and α is the contact angle between liquid water and the pore surface. After obtaining the saturation degree, capillary pressure can be derived from Eq. (3), and the corresponding RH can be obtained using

$$h = \exp\left(\frac{p_c M_w}{\rho_l RT}\right) \tag{4}$$

3. Results

3.1. Loading and deflection tests

To ensure the enclosure can be utilized as a reinforcement spacer, load and deflection tests were conducted in accordance with the British Standard BS 7973–1 [31]. The enclosure was designed to support reinforcement with a diameter of not greater than 16 mm and cover depth in the range of 15 to 50 mm which is categorized under the light spacer category. The specification for such a spacer (Annex A.1.3.2, BS 7973–1) requires a deflection of no >1 mm when it is loaded at 0.25 kN for 10 mins. This requirement was checked by attaching an 8 mm diameter ribbed steel bar with a flat gauge plate placed below the enclosure. Load-deflection tests with an Instron universal testing machine and corresponding height measurements recorded a maximum deflection of 0.05 mm when the enclosure was loaded at 0.25 kN for 10 min. Furthermore, no signs of cracking were observed.

3.2. Precision of humidity measurements

Figs. 5 and 6 present changes in measured relative humidity against time to understand the effects of increasing/decreasing moisture on the precision of RFID MEMS sensors. Plots are separated into three different relative humidity ranges. Although measurements were obtained every 5 s, only one data point per minute is plotted to enhance clarity. The measurements show that the sensors have good precision, achieving a maximum difference of ± 2 % once the readings had reached equilibrium. Similar trends were observed at 86 % relative humidity with a difference of ± 1 % between measurements. When the sensors were placed in incubators at decreasing relative humidity, the results (Fig. 6) obtained also showed good precision with a maximum difference of ± 1 % between readings at equilibrium. This indicates that the RFID MEMS sensors provide reproducible results within the desired sensing range of 70 to 90 % relative humidity. Furthermore, the results are consistent with the sensor manufacturer specifications of ± 3.5 % accuracy for the sensing ranging from 70 to 90 % relative humidity.

Nevertheless, the results show a larger deviation for measurements at high relative humidity close to saturation. For example, a 5 to 6 % deviation in the measurements from the expected value was observed at 93 % relative humidity. This deviation could have resulted from high capillary forces and stiction [39–41]; where attractive forces have exceeded counteracting forces affecting the functionality of polymer dielectric planar capacitor structure sensors. In addition, condensation on the sensor could have contributed to such effects. These observations are similar to other experimental studies conducted with MEMS devices exposed to humid environments. Patton et al. [39] observed a reduction in the performance of polysilicon MEMS cantilever motors at relative humidity above 70 % due to high capillary forces and stiction. Birleanu et al. [42] measured a rise in pull-off forces between aluminium bridges and silicon substrate during an increase in relative humidity from 40 to 70 %. To improve performance at high humidity environments, a 5-point calibration could be conducted with measurements obtained at relative humidity above 93 %. However, it is also important to note the limitations of using saturated salt solutions for providing accurate control environments above 90 % relative humidity.

3.3. Rate of response

The changes in relative humidity against time are presented in Figs. 7 and 8 to understand the effects of increasing/decreasing moisture on the time required to detect the expected relative humidity. Plots were separated into four different relative humidity ranges with arrows to indicate the response time. This was established as the time required to stabilize at the relative humidity of the surrounding environment from a starting controlled laboratory condition of 55 ± 5 % RH. As before, measurements were obtained every 5 s, but only one data point per minute was plotted to enhance clarity.

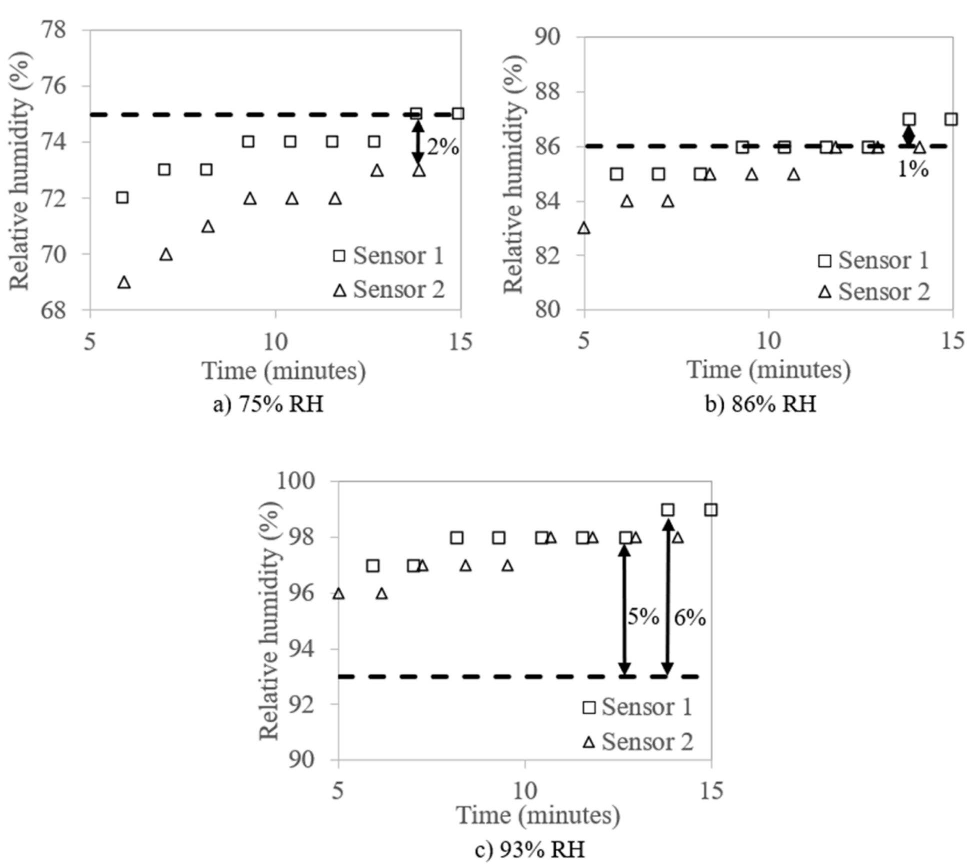

Fig. 5. Evaluating the precision of RFID MEMS at increasing humidity by placing the sensor in incubators containing saturated salts in the order of sodium chloride (75 % RH), potassium hydrogen sulphate (86 % RH) and potassium nitrate (93 % RH).

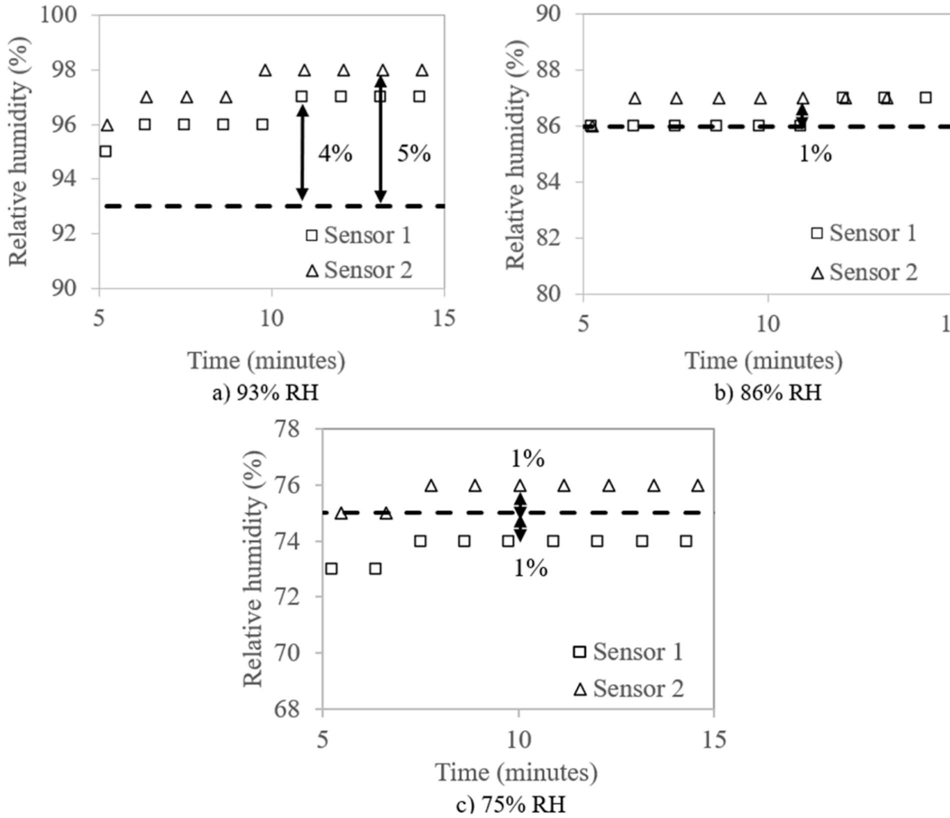

Fig. 6. Evaluating the precision of RFID MEMS at decreasing humidity by placing sensors in incubators containing saturated salts in the order of potassium nitrate (93 % RH), potassium hydrogen sulphate (86 % RH) and sodium chloride (75 % RH).

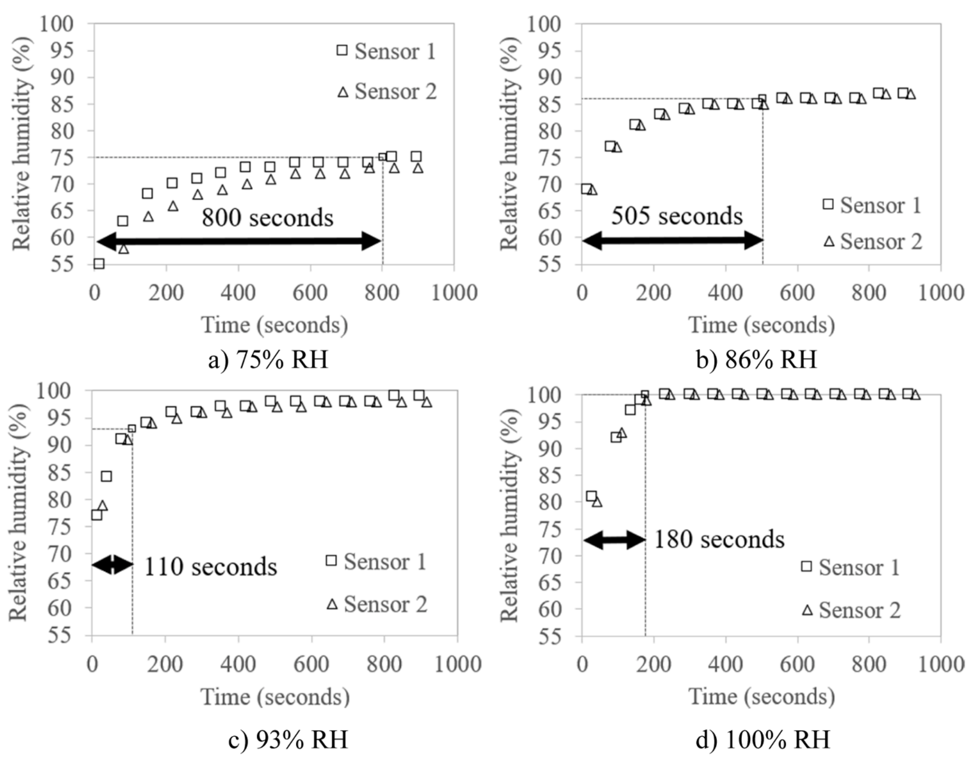

Fig. 7. Examining the rate of response of RFID MEMS at increasing humidity by placing sensors in incubators containing saturated salts in the order of sodium nitrate (75 % RH), potassium hydrogen sulphate (86 % RH), potassium nitrate (93 % RH) and water (100 % RH).

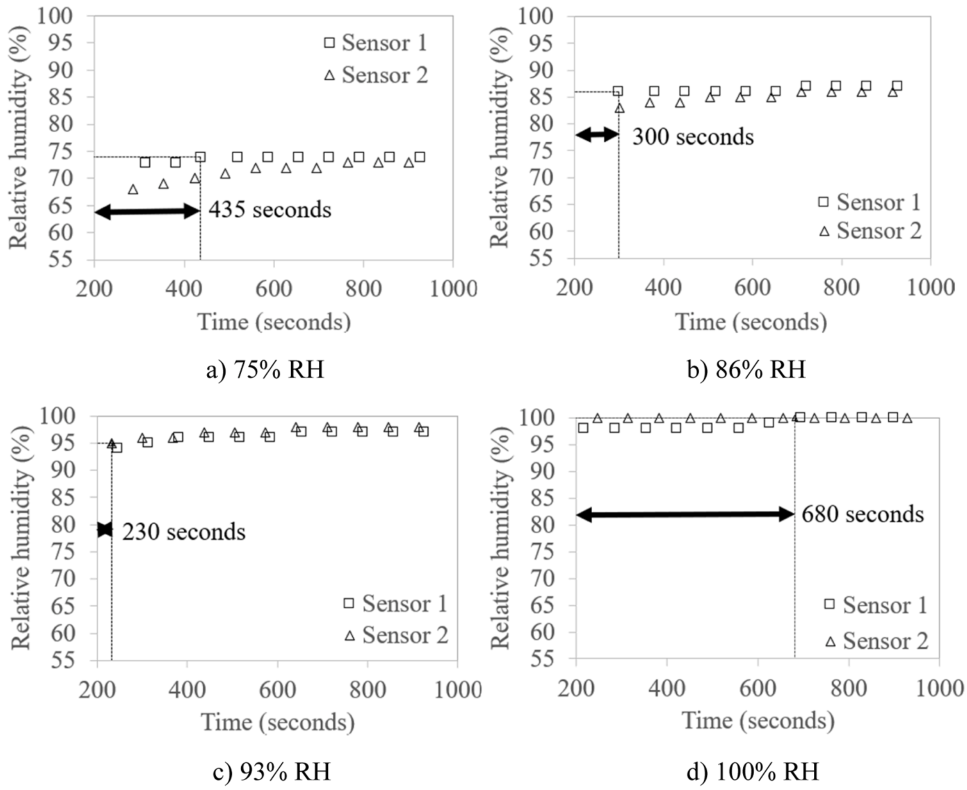

Fig. 8. Examining the rate of response of RFID MEMS at decreasing humidity by placing sensors in incubators containing water (100 % RH), saturated potassium nitrate (93 % RH), potassium hydrogen sulphate (86 % RH) and sodium nitrate (75 % RH) salt solutions.

Measurements obtained suggest lesser time was required for MEMS sensors to stabilize at higher relative humidity. This can be observed with the detection times of 800 s for 75 % RH, 505 s for 86 % RH, 110 s for 93 % RH and 180 s for 100 % RH. The reduction in detection times can be influenced by an increase in the moisture content of the surrounding environment. Furthermore, it is interesting to note that a longer time was required to detect 100 % RH compared to 93 % RH. This could be caused by moisture accumulating on the sensing element resulting in stiction affecting its performance and response.

By placing sensors in incubators at decreasing relative humidity, a similar trend of reduction in detection time at higher relative humidity was observed. The obtained detection times were 435 s for 75 % RH, 300 s for 86 % RH and 180 s for 93 % RH. However, the sensor required 680 s to detect 100 % RH which could be resulted by a high amount of moisture present in the environment affecting the performance of polymer dielectric planar capacitor structure sensors.

3.4. Wireless communication range

Fig. 9 presents the measured communication range against submergence time in water and orientation angle for mortar and concrete specimens of different cover depths to understand the effects of moisture, aggregate content and directional placement. Near identical communication distances were measured with replicate samples; thus, average values were presented for clarity.

On the one hand, the results in Fig. 9a show a communication range of 120 mm for the mortar with a 50 mm cover compared to 115 mm for concrete with a 50 mm cover, prior to submergence in water. These observations suggest that the presence of coarse aggregates and the increase in aggregate content in the concrete specimen can cause attenuation and result in a loss of signal strength. Moreover, a small decrease in communication range was observed after a submergence time of 60 min. This suggests that the increase in moisture content can reduce the antenna inductance and dielectric constant and increase its electric

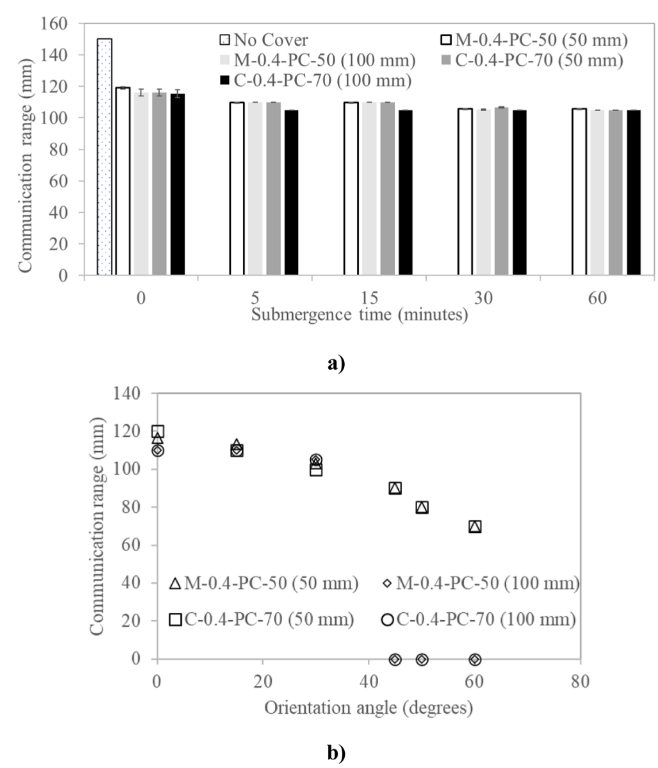

Fig. 9. Effect of a) cover thickness and moisture; and b) orientation angle between RFID MEMS sensor and reader, on maximum communication range.

conductivity [43,44].

On the other hand, it is interesting to note that an increase in cover depth has not significantly affected the overall communication distance between the sensor and reader. Both concrete and mortar specimens with 50 mm and 100 mm cover depth had a maximum communication distance of 115 ± 5 mm. These findings are in agreement with radio frequency measurements obtained for cementitious materials [45]. At frequencies below 100 MHz, attenuation in cementitious materials is similar to free space; hence, communication distance and signal strength will not be considerably affected.

Fig. 9b shows that an increase in the orientation angle between the RFID reader and sensor will reduce the overall communication range. By tilting the RFID MEMS sensor 15° away from the horizontal plane both mortar and concrete specimens with 50 mm and 100 mm cover depth had a maximum communication distance of 110 mm. At 30° orientation, the mortar and concrete specimens with 50 mm cover depth had a communication distance of 100 mm. On the other hand, a communication distance of 95 mm was measured for mortar and concrete specimens with 100 mm cover depth. Increasing the orientation angle to 45°, both mortar and concrete samples with 100 mm cover depth were undetectable. This can be attributed to a polarization mismatch between the transmitting and receiving antenna. These findings agree with experimental studies conducted with RFID sensors and transponders operating at the radio frequency range of 13.56 MHz [46,47].

3.5. Monitoring RH change in concrete

Fig. 10 shows the change in internal relative humidity at the steel-concrete interface against elapsed time, for concrete specimens with different w/c ratios and curing age, subjected to 50 °C oven drying. Measurements were started once the desired curing age had been achieved and before subjecting samples to 50 °C oven drying. Data obtained show a tendency for moisture to retain in specimens with longer curing age and lower w/c ratio. At approximately 283 hours, the internal relative humidity measurements for samples with a w/c ratio of 0.4 w/c and 0.5 w/c cured for 3 days were 25 % and 48 %; while samples with a w/c ratio of 0.4 w/c and 0.5 w/c cured for 14 days were 37 % and 54 % respectively. These observations are plausible because denser specimens have lower porosity, finer pore structure and lower mass transport properties [48]. Thus, the overall rate of desorption decreases for denser specimens, requiring a longer time to reach equilibrium with the external environment. An anomaly in relative humidity measurements at ~133 hours as shown in Fig. 10b This might have resulted from the sudden fluctuation in temperature when moving specimens from the 50 °C oven to the ambient laboratory at 21 ± 2 °C to obtain measurements. Overall, a 2 % difference was observed between the simulated, and sensor results for 0.55 w/c sample (Fig. 10c). This could be contributed by the slight inaccuracy of the embedded sensor.

Fig. 11 presents the change in internal relative humidity against elapsed time when the 50 °C oven-dried concrete specimens were exposed to 65 % RH, 21 ± 2 °C. The overall trend suggests a greater increase in relative humidity for specimens with a higher w/c ratio and shorter curing age. Measurements acquired at 833 hours indicated an internal relative humidity for samples with w/c ratio of 0.4 w/c and 0.5 w/c cured for 3 days were 61 % and 67 %; while samples with w/c ratio of 0.4 w/c and 0.5 w/c cured for 14 days were 59 % and 57 % respectively. These findings are again related to the porosity, pore structure and mass transport properties as explained earlier[31]. Less dense specimens show a higher rate of absorption and require a shorter time to reach equilibrium with the external environment. FEM simulation was also conducted to model the corresponding wetting process, utilizing the WVSI for the wetting branch as described in Eq. (3). Overall, a 4 % difference was observed between the simulated, and sensor result for 0.55 w/c sample (Fig. 11c). This could be contributed by the slight

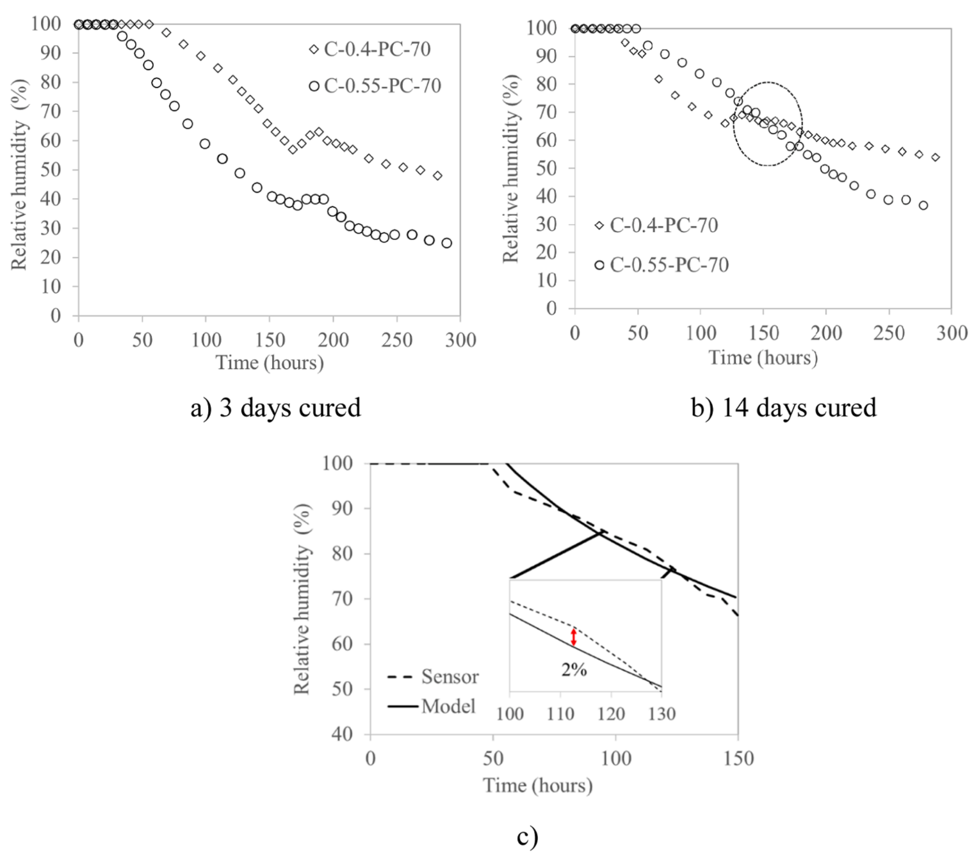

Fig. 10. Monitoring changes of internal relative humidity at the steel-concrete interface with RFID MEMS sensors in concrete specimens with 25 mm nominal cover depth during oven drying at 50 °C, along with c) the simulated variation of RH throughout the drying process for sample with w/c ratio of 0.55 cured for 14 days.

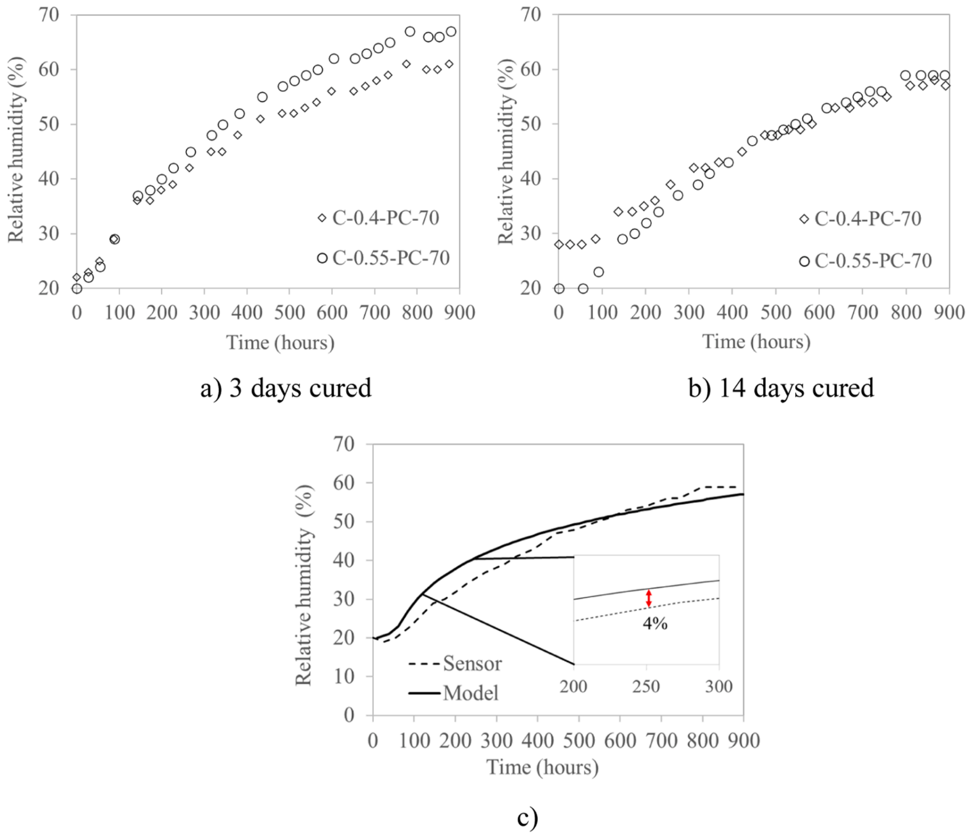

Fig. 11. Monitoring changes of internal relative humidity at the steel-concrete interface with RFID MEMS sensors in concrete specimens with 25 nominal cover depth during exposure to 65 % RH following oven drying at 50 °C, along with c) the simulated variation of RH throughout the wetting process for sample with w/c ratio of 0.55 cured for 14 days.

inaccuracy of the embedded sensor.

4. Discussion

This study demonstrates that 3D-printed enclosures can effectively shield RFID MEMS sensors from environmental exposure while preserving mechanical stability. However, sensor precision significantly declined beyond 93 % RH, primarily due to condensation-induced stiction. The loss of precision is likely caused by water accumulation on the sensing layer, which increases pull-off forces and hysteresis. This phenomenon was previously documented in polymer-based MEMS devices [49]. While these findings support the cost-effective deployment of such sensors in reinforced concrete structures, long-term durability may require additional anti-stiction measures. Future work should explore protective coatings, hydrophobic surface treatments, or dynamic self-cleaning mechanisms to mitigate moisture-related effects and further assess their impact on sensor accuracy and reliability.

Furthermore, the effects of cover depth, water-to-cement ratio and aggregate volume on RFID-based sensor communication distance were evaluated. The results indicate that these material parameters do not significantly influence signal transmission between the reader and sensor. However, in practical applications, the use of larger diameter reinforcing steel may disrupt the magnetic field generated by the sensor coil, reducing inductance and impairing power transfer efficiency which potentially diminishes communication range [50]. These findings suggest that metallurgy properties (e.g., steel composition, geometry, and electromagnetic interference) need further investigation, particularly for near-field and far-field wireless systems in reinforced concrete. Table 4 provides a comparative analysis of sensor technologies for moisture monitoring, evaluating their advancements in fabrication techniques and integration complexity. Beyond sensor performance, the reliability of wireless structural health monitoring depends not only on signal integrity but also on secure communication protocols and robust hardware architectures. Unverified datasets and vulnerable hardware implementations expose systems to adversarial manipulation, compromising real-time data integrity [51,52]. Future work should explore tamper-resistant designs and cryptographic safeguards to mitigate these risks in civil infrastructure applications.

Future Research Directions

1. Anti-stiction for MEMS Sensors

a. Develop protective coatings or hydrophobic surface treatments to reduce condensation effects

Table 4
Comparative Analysis of Sensor Technologies for Monitoring Moisture.

Technology	Piezoelectric	Capacitive	Fiber Optic	Microwave	Resistivity	RFID MEMS
Monitoring at SCI	No	No	No	No	No	Yes
Wireless operation	No	Yes	No	No	No	Yes
Operational Conditions	−15–60 °C	−40–100 °C	0–60 °C	20–40 °C	3–105 °C	−40–120 °C
Fabrication Complexity	Moderate	High (cleanroom)	Very high	Moderate	Moderate	Low
Integration Complexity	Low	Medium	High	Low	Medium	Low

b. Investigate dynamic self-cleaning mechanisms to prevent stiction and hysteresis
c. Assess long-term durability under high humidity (> 93 % RH)

2. Wireless Communication

a. Study the impact of reinforcing steel (geometry and composition) on RFID sensor performance

3. Security and Reliability

a. Implement tamper-resistant hardware designs for structural health monitoring
b. Integrate cryptographic protocols to ensure secure data transmission
c. Address vulnerabilities in real-time data integrity and adversarial threats

5. Conclusions

This study examined the feasibility of embedding RFID MEMS sensors in 3D-printed reinforcement spacers to monitor relative humidity at the steel-concrete interface (SCI) non-destructively. The main findings are as follows:

a) The 3D-printed enclosure provides sufficient protection to the embedded RFID MEMS sensor and wireless communication range. It has adequate mechanical properties to support reinforcing steel and act as a reinforcement spacer. Compared to conventional methods this innovation enables the integration of RFID MEMS sensors with 3D-printed enclosures, allowing them to function both as reinforcement spacers in concrete and as real-time monitoring devices.
b) RFID MEMS sensors provide precise and non-destructive measurements of relative humidity with a maximum difference of ± 2 % for exposure humidity up to 90 % RH. However, a reduction in precision with a deviation of 6 % was observed in environments above 93 % RH. This decline in performance may result from moisture accumulation on the sensing element, which can lead to condensation-induced stiction and increased pull-off forces.
c) The wireless communication range was not significantly affected by submerging the concrete in water or by increasing the cover depth up to 100 mm. However, a reduction in communication distance was observed when tilting the RFID MEMS sensor away from the RFID reader. This effect arises from a polarization mismatch between the transmitting and receiving antenna- a well-documented constraint in RFID systems that reduces signal coupling efficiency when antenna orientations are misaligned.
d) The proposed method can detect changes in moisture state at the SCI depending on the concrete type and exposure environment. A slower rate of increase (or decrease) in relative humidity was observed in concrete specimens with a lower w/c ratio or longer curing age, when subjected to wetting (or drying). This is attributed from the denser microstructure, which impedes moisture transport. These findings can enable composition-specific corrosion risk evaluation by providing quantitative relationships between material properties, environmental exposure, and moisture dynamics at the SCI.

CRediT authorship contribution statement

Jia-Xiang Liew: Writing – review & editing, Writing – original draft, Visualization, Validation, Methodology, Formal analysis, Data curation, Conceptualization. **Hong Wong:** Writing – review & editing, Supervision, Conceptualization.

Declaration of competing interest

The authors declare that they have no known competing financial interests or personal relationships that could have appeared to influence the work reported in this paper.

Acknowledgements

This work was published with support from the Imperial College London Open Access Fund. We gratefully acknowledge the valuable input, feedback and comments provided by Professor Nick Buenfeld, as well as the technical assistance from Andrew Morris and Les Clark in the laboratory work.

Data availability

Data will be made available on request.

References

[1] H.J. Wierig, Longtime studies on the carbonation on concrete under normal outdoor exposure, in: Proceedings of Seminar Durability of Concrete Structures Under Normal Outdoor Exposure, 1984, pp. 239–249.
[2] C. Thiel, J. Kratzer, B. Grimm, T. Kränkel, C. Gehlen, Effect of internal moisture and outer relative humidity on concrete carbonation, CivilEng 3 (2022) 1039–1052, https://doi.org/10.3390/civileng3040058.
[3] M. Liu, X. Ju, L. Wu, Q. Guo, H. Wang, W. Zhang, Carbonation depth model for loaded reinforced concrete (RC) beams under time-dependent relative humidity conditions, J. Build. Eng. 65 (2023) 105618, https://doi.org/10.1016/j.jobe.2022.105618.
[4] T. Du, Y. Cai, Y. Guo, J. Chen, S. Chen, M. Yuan, F. Qu, Time-dependent model for in-situ concrete carbonation depth under combined effects of temperature and relative humidity, Case Stud. Constr. Mater. 22 (2025) e04379, https://doi.org/10.1016/j.cscm.2025.e04379.
[5] A. Leemann, P. Nygaard, J. Kaufmann, R. Loser, Relation between carbonation resistance, mix design and exposure of mortar and concrete, Cem. Concr. Compos 62 (2015) 33–43, https://doi.org/10.1016/j.cemconcomp.2015.04.020.
[6] U.M. Angst, M.R. Geiker, M.C. Alonso, R. Polder, O.B. Isgor, B. Elsener, H. Wong, A. Michel, K. Hornbostel, C. Gehlen, R. François, M. Sanchez, M. Criado, H. Sørensen, C. Hansson, R. Pillai, S. Mundra, J. Gulikers, M. Raupach, J. Pacheco, A. Sagüés, The effect of the steel–concrete interface on chloride-induced corrosion initiation in concrete: a critical review by RILEM TC 262-SCI, Mater. Struct 52 (2019), https://doi.org/10.1617/s11527-019-1387-0.
[7] U.M. Angst, M.R. Geiker, A. Michel, C. Gehlen, H. Wong, O.B. Isgor, B. Elsener, C. M. Hansson, R. François, K. Hornbostel, R. Polder, M.C. Alonso, M. Sanchez, M. J. Correia, M. Criado, A. Sagüés, N. Buenfeld, The steel–concrete interface, Mater. Struct./Mater. Constr. 50 (143) (2017), https://doi.org/10.1617/s11527-017-1010-1, 24.
[8] J. Wen, Y. Wan, C. Xu, Y. Yang, A review of new methods for measuring saturation of concrete and its impact on concrete properties, J. Build. Eng. 96 (2024) 110664, https://doi.org/10.1016/j.jobe.2024.110664.
[9] S. Li, Z. Jin, H. Chang, Y. Gao, Oxygen diffusion into unsaturated seawater and sea sand concrete and its effect on non-uniform corrosion of steel bars, J. Build. Eng. 84 (2024) 108665, https://doi.org/10.1016/j.jobe.2024.108665.
[10] S. Mundra, E. Rossi, L. Malenica, M. Pundir, U.M. Angst, Precipitation of corrosion products in macroscopic voids at the steel–concrete interface: observations, mechanisms and research needs, Mater. Struct 58 (2025) 90, https://doi.org/10.1617/s11527-025-02614-z.
[11] J. Pavlik, V. Tydlitat, R. erny, T. Kleka, P. Bouka, P. Rovnanikova, Application of a microwave impulse technique to the measurement of free water content in early hydration stages of cement paste, Cem. Concr. Res 33 (2003) 93–102.
[12] G. Klysz, J.-P. Balayssac, Determination of volumetric water content of concrete using ground-penetrating radar, Cem. Concr. Res 37 (2007) 1164–1171.
[13] P.F. de, J. Cano-Barrita, A.E. Marble, B.J. Balcom, J.C. García, I.V. Masthikin, M.D. A. Thomas, T.W. Bremner, Embedded NMR sensors to monitor evaporable water loss caused by hydration and drying in Portland cement mortar, Cem. Concr. Res 39 (2009) 324–328, https://doi.org/10.1016/j.cemconres.2009.01.011.
[14] A.Q. Nguyen, G. Klysz, F. Deby, J.-P. Balayssac, Evaluation of water content gradient using a new configuration of linear array four-point probe for electrical resistivity measurement, Cem. Concr. Compos 83 (2017) 308–322.
[15] L. Biondi, M. Perry, J. McAlorum, C. Vlachakis, A. Hamilton, Geopolymer-based moisture sensors for reinforced concrete health monitoring, Sens. Actuators. B Chem 309 (2020) 127775, https://doi.org/10.1016/j.snb.2020.127775.
[16] A. Norris, M. Saafi, P. Romine, Temperature and moisture monitoring in concrete structures using embedded nanotechnology/microelectromechanical systems (MEMS) sensors, Constr. Build. Mater 22 (2008) 111–120, https://doi.org/10.1016/j.conbuildmat.2006.05.047.
[17] T.U. Mohammed, H. Hamada, A. Hasnat, M.A. Al Mamun, Corrosion of steel bars in concrete with the variation of microstructure of steel-concrete interface, J. Adv. Concr. Technol. 13 (2015) 230–240, https://doi.org/10.3151/jact.13.230.
[18] T. Sokoll, A.F. Jacob, Self-oscillating measurement system for in situ-monitoring moisture in buildings, IEEe Trans. Instrum. Meas 63 (2014) 2911–2918, https://doi.org/10.1109/TIM.2014.2318931.

[19] H. Zhang, J. Li, F. Kang, Real-time monitoring of humidity inside concrete structures utilizing embedded smart aggregates, Constr. Build. Mater 331 (2022) 127317, https://doi.org/10.1016/j.conbuildmat.2022.127317.

[20] T. Raunima, E. Tuominen, J. Vinha, Behavior of capacitive humidity sensors in monitoring the drying of concrete walls, in: MATEC Web of Conferences, 2019 02053, https://doi.org/10.1051/matecconf/201928202053.

[21] Y.A. Villagrán Zaccardi, J.F. García, P. Huélamo, Á.A. Di Maio, Influence of temperature and humidity on Portland cement mortar resistivity monitored with inner sensors, Mater. Corros. 60 (2009) 294–299, https://doi.org/10.1002/maco.200805075.

[22] X. Lu, K. Hicke, M. Breithaupt, C. Strangfeld, Distributed humidity sensing in concrete based on polymer optical fiber, Polym. (Basel) (2021) 13, https://doi.org/10.3390/polym13213755.

[23] T. Sokoll, A.F. Jacob, Self-oscillating measurement system for in situ-monitoring moisture in buildings, IEEe Trans. Instrum. Meas 63 (2014) 2911–2918, https://doi.org/10.1109/TIM.2014.2318931.

[24] P. Mezzanotte, V. Palazzi, F. Alimenti, L. Roselli, Innovative RFID sensors for internet of things applications, IEEe J. Microw 1 (2021) 55–65, https://doi.org/10.1109/JMW.2020.3035020.

[25] F. Costa, S. Genovesi, M. Borgese, A. Michel, F.A. Dicandia, G. Manara, A review of RFID sensors, the new frontier of internet of things, Sensors 21 (2021), https://doi.org/10.3390/s21093138.

[26] M.A. Musarat, W.S. Alaloul, A.M. Khan, S. Ayub, N. Jousseaume, A survey-based approach of framework development for improving the application of internet of things in the construction industry of Malaysia, Results. Eng 21 (2024) 101823, https://doi.org/10.1016/j.rineng.2024.101823.

[27] A. Youssef, I. Halkhams, R. El Alami, mohammed Ouazzani jamil, Q. Hassan, Study and design of a microstrip patch antenna array for 2.4 GHz applications, in: International Conference on Digital Technologies and Applications (ICDTA'23), 2023, https://doi.org/10.1007/978-3-031-29857-8_31.

[28] A. Youssef, I. Halkhams, R. El Alami, mohammed Ouazzani jamil, Q. Hassan, Analysis and design of a rectangular microstrip antenna for RFID applications. Convergence of Antenna Technologies, Electronics, and AI, IGI Global, 2024, https://doi.org/10.4018/979-8-3693-3775-2.ch025.

[29] H. Zemmour, G. Baudoin, A. Diet, Soil effects on the underground-to-aboveground communication link in ultrawideband wireless underground sensor networks, IEEE Antennas Wirel. Propag. Lett. (USA) 16 (2017) 218–221.

[30] C. Strangfeld, S. Johann, M. Bartholmai, Smart RFID sensors embedded in building structures for early damage detection and long-term monitoring, Sens. (Switz.) 19 (5514) (2019), https://doi.org/10.3390/s19245514, 18.

[31] B. Standard, BS 7973-1: Spacers and Chairs for Steel Reinforcement and Their Specification, BSI Standards Publication, 2001.

[32] C09.20, ASTM C566-19 Standard Test Method for Total Evaporable Moisture Content of Aggregate by Drying, ASTM Standards, 2019.

[33] C09.20, ASTM C128-15 Standard Test Method for Relative Density (Specific Gravity) and Absorption of Fine Aggregate, ASTM Standards, 2016.

[34] J. Kim, W.J. McCarter, B. Suryanto, Cover-zone protective qualities under corrosive environments, J. Build. Eng. 33 (2021) 101618, https://doi.org/10.1016/j.jobe.2020.101618.

[35] U.M. Angst, M.R. Geiker, M.C. Alonso, R. Polder, O.B. Isgor, B. Elsener, H. Wong, A. Michel, K. Hornbostel, C. Gehlen, R. François, M. Sanchez, M. Criado, H. Sørensen, C. Hansson, R. Pillai, S. Mundra, J. Gulikers, M. Raupach, J. Pacheco, A. Sagüés, The effect of the steel–concrete interface on chloride-induced corrosion initiation in concrete: a critical review by RILEM TC 262-SCI, Mater. Struct (2019) 52, https://doi.org/10.1617/s11527-019-1387-0.

[36] G. Prakash, A. Sadhu, S. Narasimhan, J.-M. Brehe, Initial service life data towards structural health monitoring of a concrete arch dam, Struct. Control Health Monit 25 (2018) e2036, https://doi.org/10.1002/stc.2036.

[37] J.M.W. Brownjohn, P. Moyo, Monitoring of Singapore-Malaysia second link during construction, in: Proceedings of the SPIE - The International Society for Optical Engineering, SPIE-Int. Soc. Opt. Eng., Nanyang Technol. Univ., Sch. of Civil & Struct. Eng., Singapore BT - Second International Conference on Experimental Mechanics 2001, 2000, pp. 528–533, https://doi.org/10.1117/12.429633, 29 Nov.-1 Dec.

[38] C. Sun, L. Yuan, X. Zhai, F. Qu, Y. Li, B. Hou, Numerical and experimental study of moisture and chloride transport in unsaturated concrete, Constr. Build. Mater 189 (2018) 1067–1075, https://doi.org/10.1016/j.conbuildmat.2018.08.158.

[39] S.T. Patton, W.D. Cowan, J.S. Zabinski, Performance and reliability of a new MEMS electrostatic lateral output motor, in: 37th Annual IEEE International Reliability Physics Symposium, IEEE, US Air Force Res. Lab., Wright-Patterson AFB, OH, United States BT - 1999 IEEE International Reliability Physics Symposium Proceedings. 37th Annual 1999, 1999, pp. 179–188, https://doi.org/10.1109/RELPHY.1999.761610, 23-25 March.

[40] Y. Li, Challenges and issues of using polymers as structural materials in MEMS: a review, J. Microelectromech. Syst. 27 (2018) 581–598, https://doi.org/10.1109/JMEMS.2018.2837684.

[41] K. Komvopoulos, Adhesion and friction forces in microelectromechanical systems: mechanisms, measurement, surface modification techniques, and adhesion theory, J. Adhes. Sci. Technol 17 (2003) 477–517, https://doi.org/10.1163/15685610360554384.

[42] C. Birleanu, M. Pustan, F. Rusu, C. Dudescu, R. Muller, A. Baracu, Relative humidity effect on pull-off forces in MEMS flexible structures measured by AFM. 2017 Symposium on Design, Test, Integration and Packaging of MEMS/MOEMS (DTIP), Piscataway, NJ, USA, 2017, 8.

[43] N.M. Faudzi, A.A. Azlan, A.R. Razali, N.H.A. Rahman, A.A. Manaf, A. Ibrahim, A. M. Mozi, Moisture impact analysis on NFC tag antennas, in: 2023 6th International Conference on Applied Computational Intelligence in Information Systems (ACIIS), 2023, pp. 1–5, https://doi.org/10.1109/ACIIS59385.2023.10367415.

[44] R. Mghaiouini, A. Elmlouky, R. El Moznine, M. Monkade, A. El Bouari, The influence of the electromagnetic field on the electric properties of water, Mediterr. J. Chem. 10 (2020) 507–515.

[45] D. Daly, T. Melia, G. Baldwin, Concrete embedded RFID for way-point positioning, in: 2010 International Conference on Indoor Positioning and Indoor Navigation, 2010, pp. 1–10, https://doi.org/10.1109/IPIN.2010.5647220.

[46] H.M. Lu, C. Goldsmith, L. Cauller, J.-B. Lee, MEMS-based inductively coupled RFID transponder for implantable wireless sensor applications, IEEE Trans Magn 43 (2007) 2412–2414, https://doi.org/10.1109/TMAG.2007.893802.

[47] A. Sakonkanapong, C. Phongcharoenpanich, Near-field HF-RFID and CMA-based circularly polarized far-field UHF-RFID integrated tag antenna, Int. J. Antennas. Propag 2020 (2020) 6427157, https://doi.org/10.1155/2020/6427157.

[48] M.R. Nokken, R.D. Hooton, Dependence of rate of absorption on degree of saturation of concrete, Cem. Concr. Aggreg. 24 (2002) 20–24.

[49] T. Lai, M. Chen, Y. Zhang, Contact time dependence of adhesion force at silica/silica interface on AFM: influence of relative humidity and contact history, Appl, Surf, Sci 600 (2022) 154175, https://doi.org/10.1016/j.apsusc.2022.154175.

[50] J. Grosinger, Robustly operating: passive near-field communication systems in metal environments, IEEe Microw, Mag 24 (2023) 30–39, https://doi.org/10.1109/MMM.2022.3233508.

[51] M.M. Kermani, R. Azarderakhsh, S. Bayat-Sarmadi, Reliable hardware architectures for efficient secure hash functions ECHO and fugue, in: Proceedings of the 15th ACM International Conference on Computing Frontiers, Association for Computing Machinery, New York, NY, USA, 2018, pp. 204–207, https://doi.org/10.1145/3203217.3203259.

[52] M. Mozaffari-Kermani, S. Sur-Kolay, A. Raghunathan, N.K. Jha, Systematic poisoning attacks on and defenses for machine learning in healthcare, IEEe J. Biomed, Health Inf. 19 (2015) 1893–1905, https://doi.org/10.1109/JBHI.2014.2344095.